21-MeV Alpha-Particle Scattering on $A=58$–64 Targets*

C. B. FULMER
Oak Ridge National Laboratory, Oak Ridge, Tennessee
AND
J. BENVENISTE
Aerosapce Corporation, San Bernardino, California
AND
A. C. MITCHELL
Lawrence Radiation Laboratory, University of California, Livermore, California
(Received 30 August 1967)

Cross sections for 21-MeV α elastic and inelastic scattering to the first 2+ level were measured at 3° intervals between 30° and 166° for ^{58}Fe, ^{58}Ni, ^{62}Ni, ^{64}Ni, and ^{64}Zn. Both the elastic and inelastic scattering data exhibit well-defined oscillations which obey the Blair phase rule throughout the angular range. Optical-model fits to the elastic scattering data were found at intervals corresponding to the half-wavelength rule for a wide range of real-well depth. Analysis of the data indicates that the scattering is concentrated in the nuclear surface but is also sensitive to the interior of the nuclear potential. Distorted-wave calculations of the inelastic angular distributions with parameters obtained from optical-model analysis of the inelastic scattering data gave good agreement with the data in the forward hemisphere, although good agreement was not generally obtained at large angles, where the inelastic scattering cross sections are comparable to the elastic scattering cross sections. Comparison of the inelastic data with distorted-wave calculations does not remove the ambiguity of the optical-model potential.

INTRODUCTION

THE nuclear optical model yields a reasonably good description of α-particle elastic scattering in the medium-energy region, in spite of some well-known ambiguities in the parameters found by optical-model analyses of experimental data. It has been suggested[1] that the ambuguity, particularly of the real-well depth, is attributable to a dependence of α elastic scattering on the nuclear surface but not the interior. Subsequently, it was demonstrated that when the wavelength of the α particle is large, the scattering is also sensitive to the interior of the nuclear potential.[2] More recently, it has been suggested[3] that ambiguities in the optical-model potential for α particles can be removed by analysis of inelastic 2+ scattering data. Distorted-wave calculations of 43-MeV inelastic scattering[4] with parameters obtained from optical-model analysis of elastic-scattering data have been found to give good agreement with experiment.

In the study reported here, measurements of elastic and inelastic scattering of 21-MeV α particles were made for a wide range of angles. This was done to extend the data at lower bombarding energy and to study trends in the optical-model paremeters and the range of validy of the distorted-waves theory. The data also provide a test, at lower bombarding energy, of some of the other theories of α scattering.

Targets in the $A\sim60$ region were selected because they are light enough for the elastic scattering data to exhibit well-defined structure in the angular distributions and an appreciable amount of data at higher bombarding energy exists for this mass region. The targets include a pair of $A=64$ isobars, a pair of $A=58$ isobars, and three Ni isotopes.

EXPERIMENTAL

The experiment was performed in the external α-particle beam of the variable-energy cyclotron of the Lawrence Radiation Laboratory at Livermore. Inasmuch as the experimental arrangement was essentially the same as that used for proton-scattering experiments reported earlier,[5,6] only a brief description is given here.

The α beam emerges from the cyclotron, and is magnetically analyzed, focused, and collimated to a diameter of $\frac{1}{8}$ in. The beam then traverses a 40-in.-diam scattering chamber and is collected in a Faraday cup that monitors beam intensity. An eight-position target changer at the center of the scattering chamber is remotely controlled. Inside the scattering chamber is a rotatable table with provisions for precisely mounting a detector such that the detector angle is remotely controlled and indicated in the control room with a precision of ±0.1 deg.

The bombarding energy is measured by scattering a portion of the incident beam by 90° and passing it through a variable absorber into a double proportional counter. An anticoincidence arrangement permits a differential range measurement of the scattered par-

* Research sponsored in part by the U. S. Atomic Energy Commission under contract with the Union Carbide Corporation.
[1] G. Igo, Phys. Rev. Letters 1, 72 (1958).
[2] R. M. Drisko, G. R. Satchler, and R. H. Bassel, Phys. Letters 5, 347 (1963).
[3] H. L. Wilson and M. B. Sampson, Phys. Rev. 137, B305 (1965).
[4] R. H. Bassel, G. R. Satchler, R. M. Drisko, and E. Rost, Phys. Rev. 128, 2693 (1962).
[5] J. Benveniste, A. C. Mitchell, and C. B. Fulmer, Phys. Rev. 129, 2173 (1963).
[6] J. Benveniste, A. C. Mitchell, and C. B. Fulmer, Phys. Rev. 133, B317 (1964).

TABLE I. Differential cross sections for elastic scattering and inelastic scattering to first state ($E^*=0.80$ MeV) for 21.10-MeV α particles on ^{58}Fe.

Elastic scattering			Inelastic scattering		
$\theta_{c.m.}$ (deg)	$\sigma(\theta)$ (mb/sr)	±%	$\theta_{c.m.}$ (deg)	$\sigma(\theta)$ (mb/sr)	±%
25.6	2270	7	32.0	9.74	30
28.8	1170	7	35.2	7.89	10
32.0	579	7	38.4	3.4	10
35.2	322	7	41.5	1.70	12
38.3	238	7	44.7	2.7	7
41.5	197	7	47.9	3.92	4
44.6	109	7	51.0	3.23	4
47.8	53.6	7	54.1	1.46	5
50.9	28.6	7	57.3	0.716	8
54.1	25.6	7	60.4	0.861	7
57.2	21.4	7	63.5	1.33	4
60.3	12.4	7	66.6	1.34	4
63.4	6.42	8	69.7	0.88	4
66.5	4.21	8	72.8	0.339	7
69.7	4.09	8	75.8	0.206	9
72.1	3.92	8	78.9	0.309	7
75.8	3.01	8	81.9	0.405	5
78.8	1.63	8	85.0	0.347	5
81.9	0.909	8	88.0	0.201	6
84.9	0.612	8	91.0	0.125	8
87.9	1.21	8	94.0	0.083	9
91.0	1.44	8	97.0	0.112	8
94.0	1.15	8	100.0	0.175	7
97.0	0.44	9	103.0	0.138	7
99.9	0.088	13	106.0	0.119	8
102.9	0.15	13	108.9	0.064	11
105.9	0.29	12	111.8	0.032	14
108.8	0.39	9	114.8	0.029	15
111.8	0.35	10	117.7	0.061	11
114.7	0.26	12	120.6	0.084	10
117.6	0.11	13	123.5	0.101	9
120.5	0.052	20	126.4	0.078	11
123.4	0.035	20	129.3	0.049	13
126.3	0.040	20	132.1	0.024	18
129.2	0.091	15	135.0	0.017	22
132.1	0.099	15	137.9	0.025	18
134.9	0.11	15	140.7	0.034	14
137.8	0.099	15	143.5	0.045	14
140.6	0.085	15	146.4	0.057	13
143.5	0.050	20	149.2	0.038	15
146.3	0.011	30	152.0	0.022	22
149.2	0.0207	30	154.8	0.032	18
152.0	0.025	30	157.6	0.036	15
154.8	0.030	30	160.4	0.045	14
157.6	0.044	30	163.2	0.045	14
160.4	0.044	30	166.0	0.038	15
163.2	0.040	30			
166.0	0.042	30			

TABLE II. Differential cross sections for elastic scattering and inelastic scattering for first excited state ($E^*=1.452$ MeV) for 21.08-MeV g particles on ^{58}Ni.

Elastic scattering			Inelastic scattering		
$\theta_{c.m.}$ (deg)	$\sigma(\theta)$ (mb/sr)	±%	$\theta_{c.m.}$ (deg)	$\sigma(\theta)$ (mb/sr)	±%
25.6	3050	5	32.1	8.00	8
28.8	1810	5	35.2	7.28	7
32.0	895	5	38.4	5.18	7
35.2	492	5	41.6	2.75	8
38.3	313	5	44.8	1.94	7
41.5	242	5	47.9	2.62	5
44.6	153	5	51.1	3.01	4
47.8	80.8	5	54.2	2.15	4
50.9	45.3	5	57.3	1.29	5
54.1	35.7	5	60.4	0.80	5
57.2	32.8	5	63.6	1.90	5
60.3	24.6	5	66.7	1.22	5
63.4	15.7	5	69.7	1.17	4
66.5	7.85	6	72.8	0.72	6
69.7	5.73	6	75.9	0.40	6
72.1	5.43	6	79.0	0.24	8
75.8	5.04	6	82.0	0.33	6
78.8	3.65	6	85.1	0.39	6
81.9	2.19	6	88.1	0.40	5
84.9	1.57	6	91.1	0.28	6
87.9	1.43	6	94.1	0.18	6
91.0	1.40	6	97.1	0.15	6
94.0	1.31	6	100.1	0.076	8
97.0	0.75	6	103.1	0.168	6
99.9	0.416	6	106.0	0.191	6
102.9	0.23	7	109.0	0.146	6
105.9	0.27	7	111.9	0.096	8
108.8	0.50	6	114.8	0.074	9
111.8	0.58	6	117.8	0.052	11
114.7	0.46	7	120.7	0.071	10
117.6	0.32	7	123.6	0.111	8
120.5	0.16	8	126.5	0.135	7
123.4	0.077	12	129.3	0.132	7
126.3	0.042	15	132.2	0.116	8
129.2	0.071	12	135.1	0.075	10
132.1	0.16	10	137.9	0.043	9
134.9	0.25	7	140.8	0.036	14
137.8	0.26	7	143.6	0.045	12
140.6	0.23	8	146.4	0.085	11
143.5	0.16	9	149.2	0.074	11
146.3	0.097	10	152.1	0.097	9
149.2	0.032	15	154.9	0.112	8
152.0	0.020	20	157.7	0.079	10
154.8	0.052	15	160.5	0.107	8
157.6	0.048	15	163.3	0.119	8
160.4	0.14	12	166.1	0.090	10
163.2	0.12	12			
166.0	0.11	12			

ticles. A correction for absorption in the scatterer is made prior to the application of the range-energy relations. A final correction for the energy lost to the recoiling nucleus yields the bombarding energy. The proportional counters are backed by a silicon *p-n* junction diode. After the range has been measured, enough absorber is left in to allow only a small fraction of the incident energy to be deposited in the silicon diode. Pulses from this detector are fed into a "continuous energy monitor," a device which measures the average height of input pulses and yields a continuously visible meter reading. Sensitivity checkes show that in the course of a run the bombarding energy is kept constant within ±0.1%.

The targets were all self-supporting foils prepared by the Isotopes Division of the Oak Ridge National Laboratory. The ^{64}Ni foil was enriched to 99.8%, while the ^{64}Zn foil was 99.85% pure. The isotopic assay of the other foils, as determined by the Isotopes Division of ORNL, is as follows:

	^{54}Fe	^{56}Fe	^{57}Fe	^{58}Fe	
^{58}Fe target	0.9%	18.7%	2.0%	78.4%	
	^{58}Ni	^{60}Ni	^{61}Ni	^{62}Ni	^{64}Ni
^{58}Ni target	99.25%	0.75%	<0.01%	<0.01%	<0.01%
	^{58}Ni	^{60}Ni	^{61}Ni	^{62}Ni	^{64}Ni
^{62}Ni target	0.46%	0.81%	0.03%	98.7%	<0.01%

The foil thicknesses ranged from 0.8 mg/cm^2 for ^{58}Ni to 1.44 mg/cm^2 for ^{62}Ni.

TABLE III. Differential cross sections for elastic scattering and inelastic scattering for first excited state ($E^*=1.172$ MeV) for 21.3-MeV α particles on ^{62}Ni.

Elastic scattering			Inelastic scattering		
$\theta_{c.m.}$ (deg)	$\sigma(\theta)$ (mb/sr)	±%	$\theta_{c.m.}$ (deg)	$\sigma(\theta)$ (mb/sr)	±%
32.0	1085	3	32.1	8.6	13
32.0	1090	3	32.1	8.0	13
35.2	555	5	35.2	7.0	6
38.3	345	3	38.4	4.6	9
38.3	346	3	38.4	5.6	9
41.5	247	3	41.5	2.8	8
41.5	246	3	41.5	2.5	8
44.6	150	3	44.7	2.7	15
44.6	157	3	44.7	2.2	15
47.7	79.9	3	47.8	3.0	4
50.9	46.9	3	50.5	3.3	5
50.9	47.0	3	50.5	3.3	5
54.0	37.9	3	54.1	2.0	5
57.1	32.0	3	57.2	1.2	6
57.1	31.7	3	57.2	1.2	6
60.2	21.9	3	60.3	0.99	6
63.3	12.2	3	63.4	1.00	5
66.4	7.21	3	66.5	1.20	5
69.5	6.30	3	69.6	1.00	5
72.6	5.91	3	72.7	0.61	6
75.6	4.45	4	75.7	0.34	7
78.7	2.68	4	78.8	0.34	7
81.7	1.51	4	81.8	0.38	6
84.7	1.26	4	84.9	0.34	7
87.8	1.50	4	87.9	0.27	7
90.8	1.45	4	90.9	0.14	7
93.7	1.07	4	93.8	0.15	9
96.7	0.53	4	96.8	0.19	6
99.7	0.17	6	99.8	0.20	5
102.6	0.24	6	102.7	0.18	7
105.6	0.39	4	105.7	0.14	6
108.6	0.55	4	108.7	0.05	12
111.5	0.45	4	111.6	0.030	12
114.5	0.35	4	114.5	0.066	9
117.4	0.15	5	117.5	0.13	7
120.3	0.043	12	120.4	0.12	7
123.2	0.035	13	123.3	0.12	7
126.1	0.085	9	126.2	0.091	8
129.0	0.14	7	129.1	0.039	12
131.9	0.16	7	132.0	0.010	23
134.8	0.15	7	134.8	0.017	19
137.6	0.13	7	137.7	0.022	17
140.5	0.14	7	140.6	0.031	14
143.4	0.10	8	143.4	0.04	12
146.2	0.046	12	146.3	0.029	15
149.1	0.028	12	149.1	0.031	14
151.9	0.035	14	151.9	0.030	14
154.7	0.055	11	154.8	0.045	12
157.6	0.095	8	157.6	0.042	12
160.4	0.073	10	160.4	0.050	11
163.2	0.085	9	163.2	0.039	13
166.0	0.046	13	166.1	0.028	15

TABLE IV. Differential cross sections for elastic scattering and inelastic scattering to first excited state ($E^*=1.34$ MeV) for 21.3-MeV α particles on ^{64}Ni.

Elastic scattering			Inelastic scattering		
$\theta_{c.m.}$ (deg)	$\sigma(\theta)$ (mb/sr)	±%	$\theta_{c.m.}$ (deg)	$\sigma(\theta)$ (mb/sr)	±%
32.0	1045	3	32.1		
32.0	1052	3	32.1		
35.2	527	3	35.2	5.8	6
38.3	344	3	38.4	3.3	15
38.3	338	3	38.4	2.0	15
41.5	246	3	41.5	2.1	12
44.6	143	3	44.7	2.3	13
44.6	150	3	44.7	2.2	13
47.7	74.1	3	47.8	2.9	5
50.9	46.2	3	50.5	2.4	6
50.9	46.0	3	50.5	2.4	6
54.0	38.9	3	54.1	1.7	4
57.1	31.0	3	57.2	0.78	7
57.1	31.3	3	57.2	0.91	7
60.2	19.4	3	60.3	0.80	7
63.3	10.5	3	63.4	1.00	6
66.4	7.30	4	66.5	0.97	6
69.5	7.02	4	69.6	0.74	6
72.6	5.79	4	72.7	0.44	8
75.6	3.91	4	75.7	0.29	9
78.7	2.13	4	78.8	0.31	9
81.7	1.17	6	81.8	0.27	9
84.7	1.38	5	84.9	0.21	10
87.8	1.63	5	87.9	0.17	12
90.8	1.47	4	90.9	0.10	10
93.7	0.92	6	93.8	0.14	12
96.7	0.36	6	96.8	0.18	8
99.7	0.18	6	99.8	0.17	7
102.6	0.31	6	102.7	0.13	10
105.6	0.40	5	105.7	0.052	14
108.6	0.49	6	108.7	0.016	28
111.5	0.30	6	111.6	0.037	19
114.5	0.24	6	114.5	0.045	14
117.4	0.086	11	117.5	0.088	11
120.3	0.057	13	120.4	0.10	9
123.2	0.052	14	123.3	0.083	12
126.1	0.061	14	126.2	0.070	12
129.0	0.15	9	129.1	0.036	17
131.9	0.10	11	132.0	0.012	29
134.8	0.067	13	134.8	0.013	29
137.6	0.075	12	137.7	0.029	19
140.5	0.057	14	140.6	0.039	17
143.4	0.069	13	143.4	0.039	17
146.2	0.055	14	146.3	0.037	17
149.1	0.041	16	149.1	0.025	31
151.9	0.028	20	151.9	0.013	29
154.7	0.044	16	154.8	0.021	21
157.6	0.058	14	157.6	0.025	21
160.4	0.068	15	160.4	0.037	18
163.2	0.077	9	163.2	0.031	14
166.0	0.045	16	166.1	0.033	19

Scattered particles from the targets were detected by a counter telescope that consists of a silicon p-n junction diode preceded by a gas proportional counter with offset center wire. Pulses from the gas proportional counter (dE/dx) pulses) and from the silicon counter (E pulses) are fed into a multiplier network whose output pulses identify detected particles as protons, deuterons, or α particles. Multiplier pulses due to α particles were selected by a single-channel pulse-height analyzer and used to gate a multichannel analyzer so that only the α spectra were recorded.

Data were usually taken successively at 6° intervals. After two sweeps in which the detector angles were interleaved, data were available at 3° intervals from 30 to 165 deg. In addition to data from the targets being studied, a spectrum from Mylar was obtained at each angle. These spectra were compared with those from the metallic foils to obtain information about the carbon and oxygen impurities in the latter. This made it possible to correct the elastic scattering data at forward angles for contributions from oxygen and carbon impurities.

EXPERIMENTAL RESULTS

The results of the elastic and inelastic scattering measurements are presented in Tables I–V. The values of the incident-particle energy E_α, are calculated for the beam after it passes through half the target foil, hence E_α for ^{58}Fe is slightly different from E_α for ^{58}Ni. The ^{58}Fe and ^{58}Ni data were obtained a few months prior to those for ^{62}Ni, ^{64}Ni, and ^{64}Zn. The available beam energy was 0.2 MeV higher for the later data. The spread in bombarding energy arises from the spread in the incident beam and from the target-foil thickness. These effects combine to yield a total spread of $\Delta E_\alpha \sim 300$ keV full width at half-maximum for the data reported here.

The uncertainties shown in Tables I–V include contributions from statistics, beam-current integrator measurements, geometric factors, and target-foil impurities and irregularities. Some of the data points were repeated in the later series of measurements. The reproducibility of the measured cross sections is shown for these points in Tables III, IV, and V.

The effect of a variation in E_α is illustrated in Fig. 1. The two curves were computed using the same optical-model parameters, but with a difference of 0.9 MeV in the incident energy. The difference in absolute cross section is rather large at some angles.

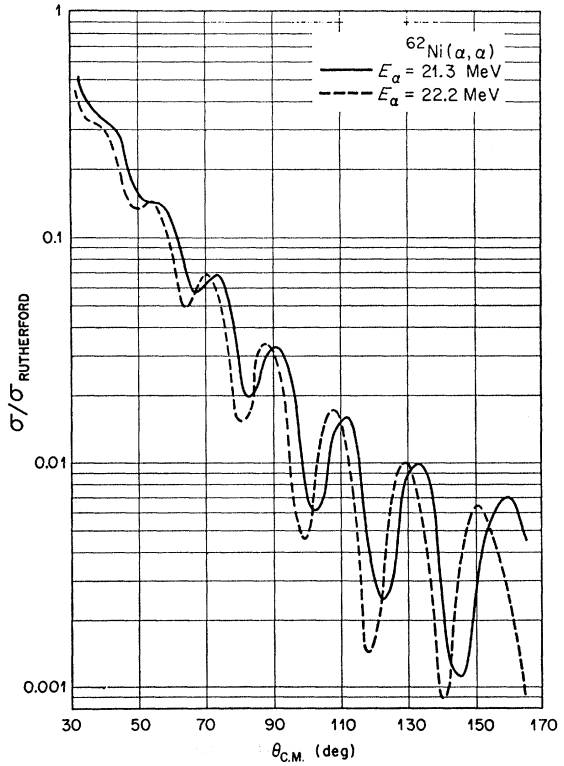

FIG. 1. Effect of energy variation on α elastic scattering. These are calculated angular distributions for optical-model parameters that gave good agreement with the experimental data for 21.3-MeV bombarding energy.

TABLE V. Differential cross sections for elastic scattering and inelastic scattering to first excited state ($E^*=0.99$ MeV) for 21.3-MeV g particles on ^{64}Zn.

Elastic scattering			Inelastic scattering		
$\theta_{c.m.}$ (deg)	$\sigma(\theta)$ (mb/sr)	±%	$\theta_{c.m.}$ (deg)	$\sigma(\theta)$ (mb/sr)	±%
32.0	1420	3	32.1	11.0	20
32.0	1452	3	32.1	8.1	20
35.2	746	3	35.2	12.3	6
38.3	468	3	38.4	7.8	8
41.5	330	3	41.5	4.8	4
44.6	197	3	44.7	4.1	9
44.6	204	3	44.7	4.3	9
47.7	107	3	47.8	5.4	5
50.9	62.1	3	50.5	5.1	4
50.9	61.2	3	50.5	5.5	4
54.0	50.1	3	54.1	3.2	4
57.1	41.9	3	57.2	1.9	6
57.1	41.6	3	57.2	1.8	6
60.2	29.9	3	60.3	1.5	6
63.3	17.0	3	63.4	2.2	6
63.3	17.0	3	63.4	2.0	6
66.4	9.83	3	66.5	2.3	4
69.5	7.70	3	69.6	1.7	4
72.6	7.05	3	72.7	1.0	5
75.6	5.47	4	75.7	0.51	6
78.7	3.73	4	78.8	0.51	6
81.7	2.42	4	81.8	0.72	6
84.7	1.95	4	84.9	0.66	6
87.8	1.80	4	87.9	0.58	6
90.8	1.71	4	90.9	0.38	6
93.7	1.25	4	93.8	0.27	8
96.7	0.61	4	96.8	0.23	6
99.7	0.32	5	99.8	0.28	6
102.6	0.46	5	102.7	0.23	7
105.6	0.59	4	105.7	0.19	6
108.6	0.66	4	108.7	0.15	6
111.5	0.47	4	111.6	0.13	7
114.5	0.34	5	114.5	0.14	7
117.4	0.150	8	117.5	0.15	7
120.3	0.049	11	120.4	0.16	7
123.2	0.066	11	123.3	0.18	7
126.1	0.14	8	126.2	0.11	8
129.0	0.18	8	129.1	0.038	13
131.9	0.20	7	132.0	0.043	13
134.8	0.18	8	134.8	0.067	11
137.6	0.15	8	137.7	0.086	10
140.5	0.13	8	140.6	0.13	8
143.4	0.059	11	143.4	0.11	8
146.2	0.028	16	146.3	0.092	9
149.1	0.033	16	149.1	0.067	10
151.9	0.063	11	151.9	0.039	14
154.7	0.10	9	154.8	0.033	15
157.6	0.17	8	157.6	0.033	15
160.4	0.14	8	160.4	0.036	15
163.2	0.13	8	163.2	0.041	14
166.0	0.066	11	166.1	0.063	12

The effect of energy spread on the data was investigated as follows: An optical-model potential was found that predicted an angular distribution that is in reasonable agreement with the data. Theoretical angular distributions were computed for the mean value of E_α and for the incident energies of $E_\alpha \pm 300$ keV. The "averaged cross section" was then calculated for each angle by

$$\sigma_{av}=\tfrac{1}{4}(2\sigma_{E_\alpha}+\sigma_{E_\alpha-300\text{ keV}}+\sigma_{E_\alpha+300\text{ keV}}).$$

The energy spread thus introduced into the averaged cross sections is about twice the experimental incident-energy spread. The two calculated angular distributions

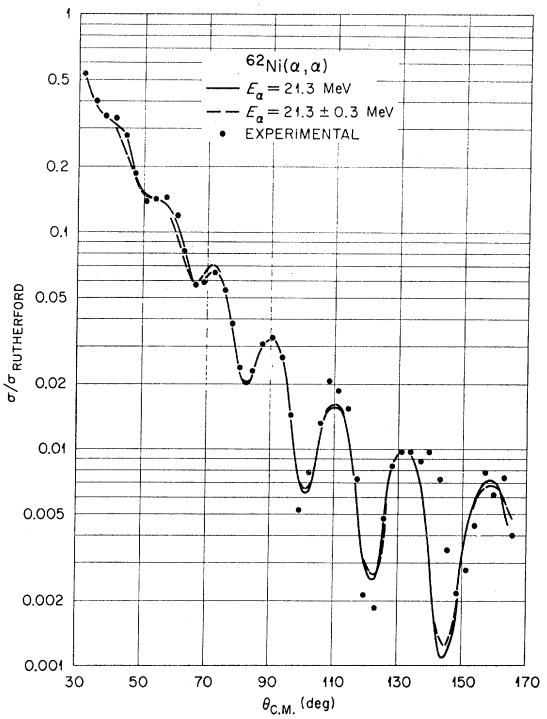

FIG. 2. Effect of energy spread on elastic α scattering.

are compared with the experimental data in Fig. 2. It is apparent from Fig. 2 that the energy spread of the incident beam does not appreciably affect the data reported here.

The scattering data for one of the targets, ^{58}Ni, are presented graphically in Fig. 3. The elastic and inelastic scattering (to the first 2+ level) exhibit well-defined diffraction patterns throughout the angular range of the data. The inelastic angular distribution is out of phase with the elastic angular distrubition, in agreement with the Blair phase rule.[7]

Rost[8] has pointed out that a minimum at 90 deg in the envelope of the angular distribution is characteristic of surface reactions that are localized to a very few partial waves. A minimum is not observed in the data shown in Fig. 3 but near 100 deg there is a change in the slope of the envelope of the inelastic angular distribution; the elastic angular distribution exhibits a less pronounced change in slope. These effects were observed in all of the α-scattering data obtained in this study. This suggests that 21-MeV α scattering is concentrated in the nuclear surface but does not exclude some contribution from the interior of the nucleus.

Neither of the isobar pairs nor the triplet of Ni isotopes exhibited unusual variations in experimental data, except for the ^{64}Ni elastic data in the 130–150° region.

[7] J. S. Blair, Phys. Rev. **115**, 928 (1959).
[8] E. Rost, Phys. Rev. **128**, 2708 (1962).

OPTICAL-MODEL ANALYSIS

The optical-model potential that was used in the analysis of the elastic scattering data reported here has the form

$$U(r)=V(r)+iW(r),$$

where

$$V(r)=-V_0 f(r,R_r,a_r),$$
$$W(r)=-W_0 f(r,R_w,a_w),$$
$$R_{r,w}=r_{r,w}A^{1/3},$$

and

$$f(r,R,a)=[1+\exp(r-R)/a]^{-1}.$$

V_0 is the central real potential, W_0 is the central imaginary potential, r_r is the radius parameter of the real potential, a_r is the diffuseness of the real potential, and r_w and a_w are the radius parameter and diffuseness, respectively, of the imaginary potential. A Coulomb potential of the form

$$V_c=(ZZ'e^2/2R_c)(3-r^2/R_c^2) \quad r\leq R_c$$
$$=ZZ'e^2/r, \quad r>R_c$$
$$R_c=r_cA^{1/3}$$

was included.

Optical-model calculations were performed with the ORNL code HUNTER[9] which has an automatic param-

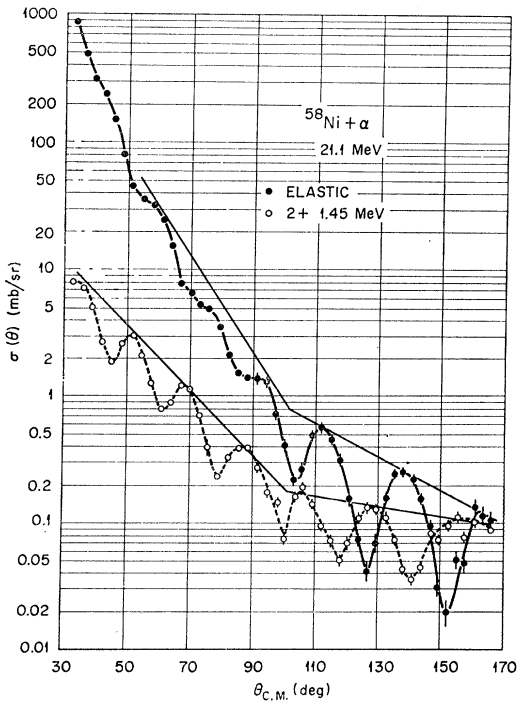

FIG. 3. ^{58}Ni elastic and inelastic scattering data. The bombarding energy was 21.08 MeV at the middle of the target foil. The curves are drawn to emphasize the features of the data. The straight lines show the envelopes of the angular distributions.

[9] R. M. Drisko (unpublished).

eter-search routine that minimizes the quantity

$$\chi^2=\sum_i [\sigma_{\text{theor}}(\theta_i)-\sigma_{\text{expt}}(\theta_i)]^2/[\Delta\sigma_{\text{expt}}(\theta_i)]^2.$$

The variable parameters in this work were V_0, W_0, r_r, a_r, r_w, and a_w. The program HUNTER permitted a search in which one or more of the six parameters were varied. It has been shown[2] that there is more than one minimum in a plot of χ^2 versus V_0 for strongly absorbed particles. Thus, the choice of starting parameters can determine the χ^2 minimum to which the parameter search will converge.

In the early phases of the analysis, several computer runs were made in which one or two of the six parameters were varied. These were followed by a run in which all six parameters were varied by the HUNTER program. In this manner potentials that minimize χ^2 were found for each of the targets for $-V_0\sim43$ MeV and for $-V_0\sim65$ MeV. These are referred to as "low-potentials" and "high potentials," respectively. The geometrical parameters, r_r, r_w, a_r, and a_w obtained for the several targets were averaged to obtain a set of low-potential geometrical parameters and a set of high-potential geometrical parameters. Then optical-model searches were made for each target with the geometrical parameters thus obtained held constant and only V_0 and W_0 varied. Thus, four potentials that minimize χ^2 were found for each target. These are low-potential free parameters, low-potential fixed geometry, high-potential free parameters, and high-potential fixed geometry. For the high-potential searches an option of the HUNTER program that required $r_r=r_w$ was used. This was found to reduce the amount of fluctuation in parameter space encountered in the searches.

Preliminary optical-model calculations indicated that better agreement could be obtained between experimental and calculated cross sections, at forward angles where Coulomb scattering is dominant, if the experimental cross sections for ^{62}Ni, ^{64}Ni, and ^{64}Zn were reduced by 10%. Thus for the remainder of the analysis the cross sections in Tables III–V were reduced by 10%. The experimental data for angles larger than 130 deg were not included in computing χ^2 and hence did not influence the results of the parameter searches.

In a few calculations the Coulomb radius parameter r_c was permitted to be varied by the parameter-search routine. No significant departure from a value of 1.4 F resulted.

The theoretical angular distributions that were calculated with the optical-model parameters obtained from the high-potential free parameters sets of parameter searches for the several targets are compared with the experimental data in Fig. 4. The optical-model parameters obtained from each of the four sets of parameter searches are summarized in Table VI. The angular distributions, obtained for each target, from the other sets of optical-model parameters shown in Table VI, are very similar to that shown in Fig. 4. Reasonably

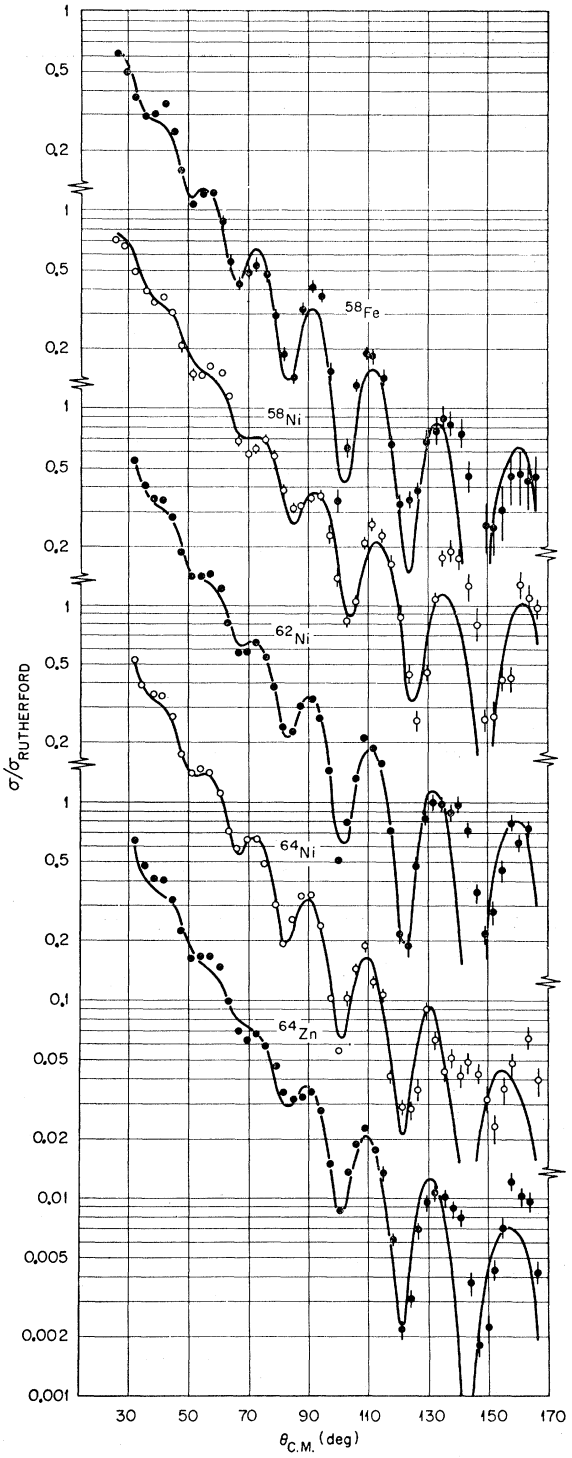

FIG. 4. Calculated elastic scattering angular distributions for the parameters from the "high-potential free-parameters" searches compared with the experimental data. The parameters are listed in Table VI.

TABLE VI. Optical-model parameters for the calculated angular distributions in Figs. 3–6. The value of the Coulomb radius parameter is 1.4 F. The total reaction cross section σ_R computed for each set of parameters is also tabulated. The values of the deformation parameter β were obtained from normalization of the distorted-wave predictions to the inelastic scattering data.

Target	V_0 (MeV)	W_0 (MeV)	r_r F	a_r F	r_w F	a_w F	σ_R mb	β
			Low potential, free-parameter search					
^{58}Fe	40.06	10.1981	1.6795	0.5307	1.7481	0.3035	1262	0.181
^{58}Ni	44.09	8.7900	1.6548	0.5149	1.7269	0.2985	1139	0.168
^{62}Ni	42.68	9.0638	1.6463	0.5078	1.7192	0.2646	1192	0.159
^{64}Ni	41.41	10.5770	1.6433	0.5205	1.6804	0.3174	1236	0.142
^{64}Zn	43.70	8.4451	1.6423	0.5183	1.7331	0.2578	1159	0.196
			Low potential, fixed-geometry search					
^{58}Fe	43.59	9.90	1.6515	0.5182	1.7211	0.2883	1220	0.178
^{58}Ni	43.90	9.6825	1.6515	0.5182	1.7211	0.2883	1151	0.167
^{62}Ni	41.58	9.3544	1.6515	0.5182	1.7211	0.2883	1210	0.155
^{64}Ni	41.27	9.6851	1.6515	0.5182	1.7211	0.2883	1238	0.137
^{64}Zn	42.55	8.9300	1.6515	0.5182	1.7211	0.2883	1175	0.190
			High potential, free-parameter search					
^{58}Fe	66.28	13.69	1.5645	0.5636	1.5645	0.5029	1274	0.178
^{58}Ni	67.43	12.78	1.5860	0.5216	1.5860	0.4093	1158	0.164
^{62}Ni	67.89	12.81	1.5550	0.5257	1.5550	0.3383	1189	0.155
^{64}Ni	64.37	13.91	1.5698	0.5282	1.5698	0.3587	1235	0.142
^{64}Zn	67.30	11.89	1.5698	0.5255	1.5698	0.3118	1171	0.188
			High potential, fixed-geometry search					
^{58}Fe	67.94	13.44	1.5690	0.5329	1.5690	0.3878	1227	0.181
^{58}Ni	69.07	13.22	1.5690	0.5329	1.5690	0.3878	1158	0.171
^{62}Ni	65.63	12.94	1.5690	0.5329	1.5690	0.3878	1216	0.155
^{64}Ni	64.24	13.74	1.5690	0.5329	1.5690	0.3878	1240	0.141
^{64}Zn	67.12	12.30	1.5690	0.5329	1.5690	0.3878	1179	0.190
^{58}Fe						Coulomb excitation		0.25
^{58}Ni						Coulomb excitation		0.19
^{62}Ni						Coulomb excitation		0.19
^{64}Ni						Coulomb excitation		0.19
^{64}Zn						Coulomb excitation		0.25

good agreement is obtained between the theoretical and experimental angular distributions both in the phase of the oscillations and in the absolute cross sections. The agreement in magnitude over the large angular range is more impressive when one notes that the cross sections are plotted as σ/σ_R in Fig. 4, and that cross sections range over five orders of magnitude. The peculiar behavior of the ^{64}Ni experimental data at angles larger than 130 deg is not understood.

In all of the analyses the structure of the theoretical angular distribution for ^{64}Zn at forward angles was observed to be less pronounced than that of the experimental data.

The low-potential optical-model parameters (Table VI) are characterized by rather large imaginary radius parameters and small imaginary diffuseness parameters. For the high-potential searches the real and imaginary radius parameters were constrained to the same values by the program option that was used. The imaginary diffuseness parameters are smaller than the real potential diffuseness parameters for the high potentials.

The value of the calculated total reaction cross section σ_R is tabulated in Table VI for each set of optical-model parameters. The various sets of parameters for each target yield values of σ_R that are reasonably constant, the largest variation is for ^{58}Fe and is less than 5%. The values of σ_R thus obtained increase with target mass for the three Ni isotopes, with about the same slope as the measured values of σ_R for 24.7-MeV α particles on $A\sim60$ nuclei that were reported by Budzanowski *et al.*[10]; the values for 21-MeV α particles listed in Table VI are $\sim10\%$ lower than the measured σ_R values for 24.7-MeV α particles reported in Ref. 10.

^{58}Ni ANALYSIS

^{58}Ni has a considerable history of experimental and theoretical studies of α scattering in the medium-energy region. We thus selected the ^{58}Ni data for the most extensive analysis in the work reported here. Our data were obtained at a bombarding energy of 21.08 MeV, which is nearer the Coulomb barrier than the bombarding energies used in most previous studies. The data also cover a wider angular range.

Optical-model parameter searches were made for a wide range of real potential well depth. For $-V_0\lesssim60$ MeV six-parameter searches were made; for $-V_0\gtrsim60$ MeV the option of the HUNTER program that requires $r_r=r_w$ was used.

[10] A. Budzanowski, K. Grotowski, J. Kuzminski, H. Niewodniczanski, A. Strazlkowski, S. Sykutowski, J. Szmider, and R. Wolski, in *Proceedings of the International Conference on Nuclear Physics, Gatlinburg, Tennessee, 1966*, edited by R. L. Becker, C. D. Goodman, P. H. Stelson, and A. Zucker (Academic Press Inc., New York, 1967).

The ^{58}Ni elastic scattering data are compared with the predictions of the calculations for six sets of parameters in Fig. 5. The parameter values are compared graphically in Fig. 6 and are tabulated in Table VII.

It is apparent from Fig. 5 that the elastic scattering data are in reasonable agreement with the predictions of potentials characterized by a large range of real-well depth. The sets of parameters are not unique. It is apparent from Fig. 6 that the values of W_0, r_w, and a_w, for the set of parameters for which $-V_0$ is 21.14 MeV, depart appreciably from the trends of the other sets of parameters. Qualitatively, the fit to the data for this potential, as shown in Fig. 5, is as good as that of the other sets of parameters.

The regions between the values of V_0 shown in Fig. 5 were investigated by using the HUNTER program to compute χ^2 for potentials characterized by intermediate values of the real-well depth. A plot of χ^2

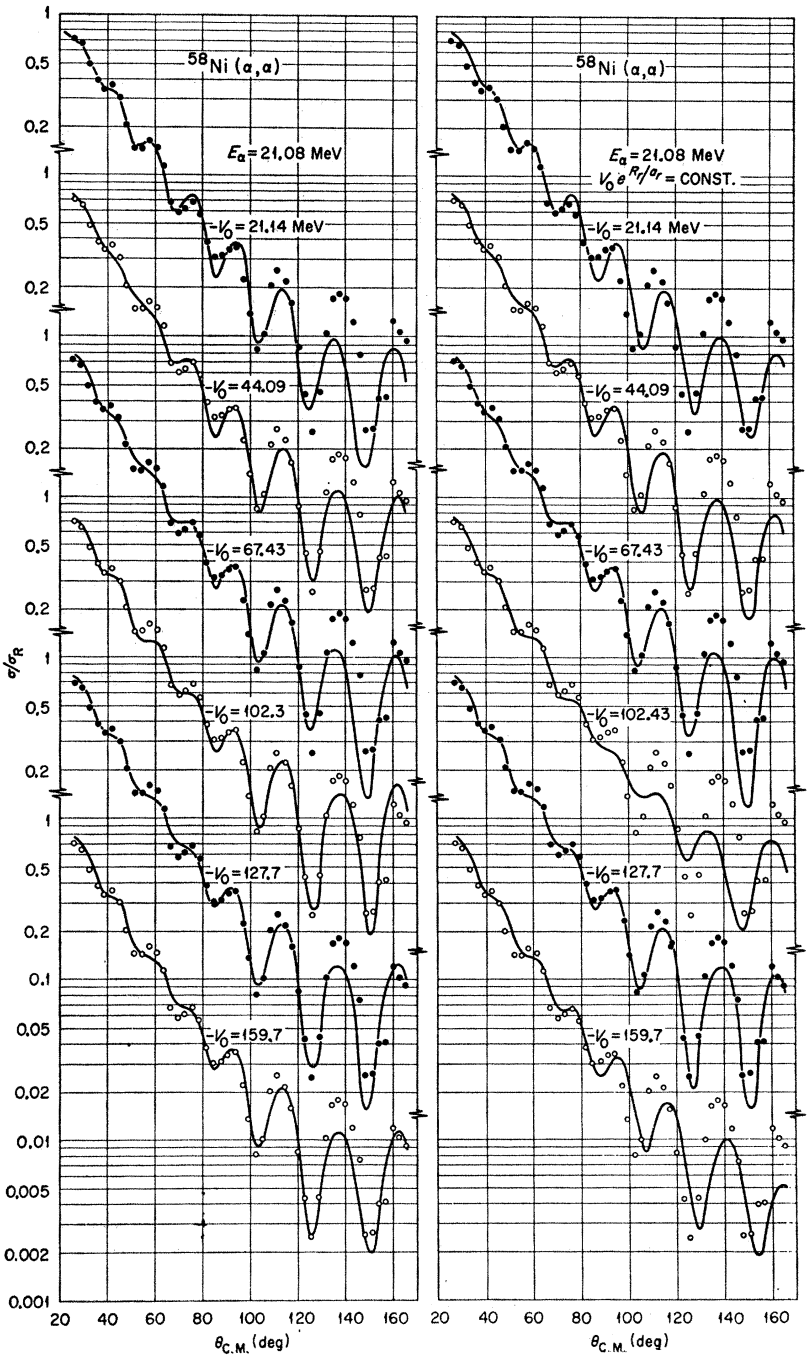

FIG. 5. Calculated elastic scattering angular distributions for six sets of parameters from ^{58}Ni analysis compared with the experimental data. The parameters are listed in Table VII and compared graphically in Fig. 6.

TABLE VII. Optical-model parameters for the calculated angular distributions in Fig. 8. The target nucleus was ^{58}Ni. These parameters were obtained by free-parameter searches with the program HUNTER. The values of χ^2, total reaction cross sections, $C_1 = V_0 \exp(R_r/a_r)$, and $C_2 = W_0 \exp(R_w/a_w)$ are also shown.

$-V_0$ (MeV)	$-W_0$ (MeV)	r_r (F)	a_r (F)	r_w (F)	a_w (F)	χ^2	σ_R (mb)	C_1/e^{10}	C_2
21.14	15.78	1.7280	0.5208	1.4147	0.8189	199	1276	219.6	$15.78e^{6.7}$
44.09	8.790	1.6548	0.5149	1.7269	0.2985	279	1156	504.8	$8.79e^{22.4}$
67.43	12.78	1.5860	0.5216	1.5860	0.4093	173	1158	349.3	$12.78e^{15}$
102.3	16.81	1.4791	0.5573	1.4791	0.1819	139	1148	134.4	$16.81e^{31.5}$
127.7	18.96	1.4900	0.5319	1.4900	0.1729	130	1165	324.4	$18.96e^{33.4}$
159.7	21.19	1.4712	0.5178	1.4712	0.2873	142	1161	432.8	$21.19e^{19.82}$

versus V_0 is shown in Fig. 7. Calculations were made at 2-MeV increments of V_0 over the region of 44–66 MeV to ensure that no intermediate minima in the curve of Fig. 7 were missed. For the 115-MeV point in Fig. 7, V_0 was held constant and the search routine of HUNTER was permitted to vary the other parameters. This resulted in a decrease in χ^2 but did not produce a good fit to the experimental data. The results of this part of the investigation show that only discrete values of the real-well depth provide good fits to the data. Thus, we conclude that 21-MeV α scattering is not insensitive to the interior of the potential. We do not wish to imply that these six families of potentials are all that could be found. McFadden and Satchler[11] have analyzed 24.7-MeV α elastic scattering data for Ni and found potentials with real-well depths >200 MeV. We investigated the possibility of a potential with $-V_0<20$ MeV and none was found that would produce as good agreement between experimental and calculated angular distributions as that shown in Fig. 5.

It has been suggested[1] that α elastic scattering is dependent only on the surface of the nucleus. This is usually expressed by the conditions

$$V_0 \exp(R_r/a_r) = C_1,$$
$$M_0 \exp(R_w/a_w) = C_2.$$

The values of C_1 and C_2 that correspond to the several sets of potentials used to calculate the angular distributions graphed in Fig. 5 are shown in Table VII. The values of C_1 are not constant but vary by many orders of magnitude. A constant value of C_1 was imposed for one series of HUNTER calculations. a_r was fixed at 0.52 F and r_r was adjusted for the various values of $-V_0$ to give the same value of C_1 as that obtained for the $-V_0=67.43$ MeV potential. The option that re-

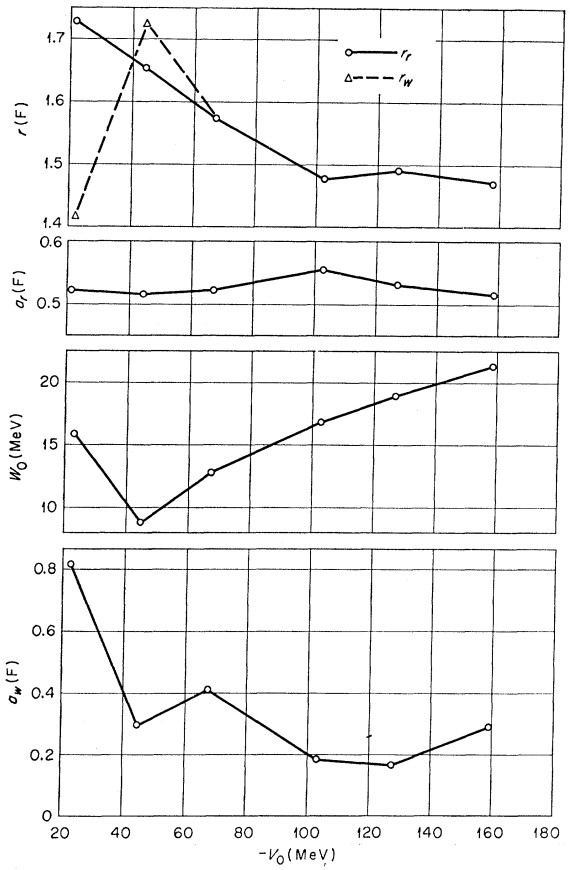

FIG. 6. Graphical comparison of parameters for six potentials that yield calculated angular distributions that fit the ^{58}Ni elastic data.

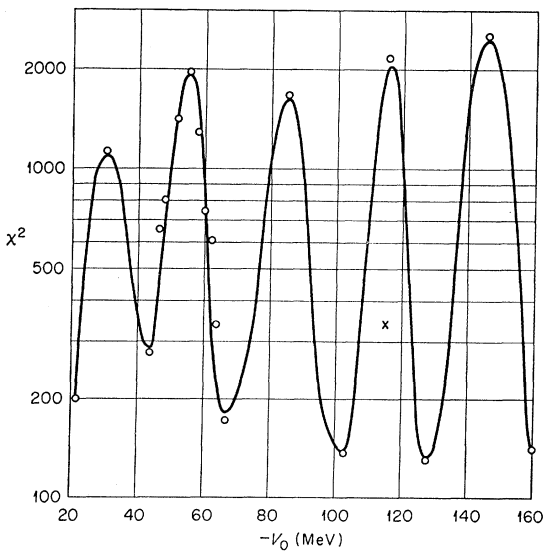

FIG. 7. χ^2 versus $-V_0$ for ^{58}Ni potentials.

[11] L. McFadden and G. R. Satchler, Nucl. Phys. 84, 177 (1966).

TABLE VIII. Results of parameter searches for which C_1=const. The target nucleus was ^{58}Ni. A constant value of a_r=0.52 F was used. Values of r_r were adjusted to give the same value of $V_0 \exp(R_r/a_r)$ as that obtained for the V_0=67.43-MeV potential. The option that requires $r_w=r_r$ was used. The HUNTER program searched on W_0 and a_w.

V (MeV)	r_r (F)	W (MeV)	a_w (F)	χ^2	σ_R (mb)	C_2/e^{15}
21.16	1.7250	7.732	0.3932	604	1132	56.4
44.09	1.6255	10.49	0.3918	347	1132	30.1
67.43	1.5860	12.93	0.3914	186	1162	25.7
102.3	1.5126	18.56	0.3148	542	1135	650
127.7	1.4824	18.52	0.2805	234	1136	4352
159.7	1.4523	23.33	0.2963	524	1136	1236

quires $r_r=r_w$ was also used and the search routine of the program HUNTER was allowed to vary W_0 and a_w. The results of this parameter search are summarized in Table VIII. In general, the values of χ^2 are larger than those obtained from the free parameter searches (Table VII) for which a constant value of C_1 was not met. The values of C_2, obtained from the sets of parameters in Table VIII, and for which C_1=const, vary by a factor of >100. The angular distributions computed with the C_1=const parameters are shown in the right half of Fig. 5. In general these angular distributions are not in as good agreement with the data as those shown in the left half of Fig. 5.

DISTORTED-WAVE CALCULATIONS

The sets of parameters obtained from many of the optical-model searches discussed in the previous sections were used to perform distorted-wave calculations of the inelastic scattering to the first excited levels of the target nuclei which for the targets studied in this investigation are all 2+ levels.

The distorted-wave calculation is described in detail in Ref. 4; it is briefly outlined as follows: The differential cross section for scattering a particle with incident momentum $\hbar\mathbf{k}_i$ and final momentum $\hbar\mathbf{k}_f$, in which the target nucleus is excited from a state of v_i to a final state v_f is given by

$$\frac{d\sigma}{d\Omega}=\left(\frac{\mu}{2\pi\hbar^2}\right)^2\left(\frac{k_f}{k_i}\right)\Sigma_{\mathrm{av}}|T_{fi}|^2,$$

where the transition amplitude is given by

$$T_{fi}=\int d\mathbf{r}\,\chi_f^{(-)}(\mathbf{k}_f,\mathbf{r})\langle v_f|V|v_i\rangle\chi_i^{(+)}(\mathbf{k}_i,\mathbf{r}).$$

The $\chi(\mathbf{k},\mathbf{r})$ are the distorted waves which describe the elastic scattering of the particle by the nucleus before and after the inelastic transitions. In zero range and in the framework of a collective-model description of the 2+ states the matrix element $\langle v_f|V|v_i\rangle$, of the transition amplitude contains a term $f_l(r)$ which is the product of the root-mean-square nuclear deformation β and the derivative of the nuclear potential $U(r)$. The latter is defined by the optical-model parameters used, which were determined from the analysis of the elastic scattering data. Normalization of the calculated to the experimental angular distribution of the 2+ level gives a measure of the deformation parameter β.

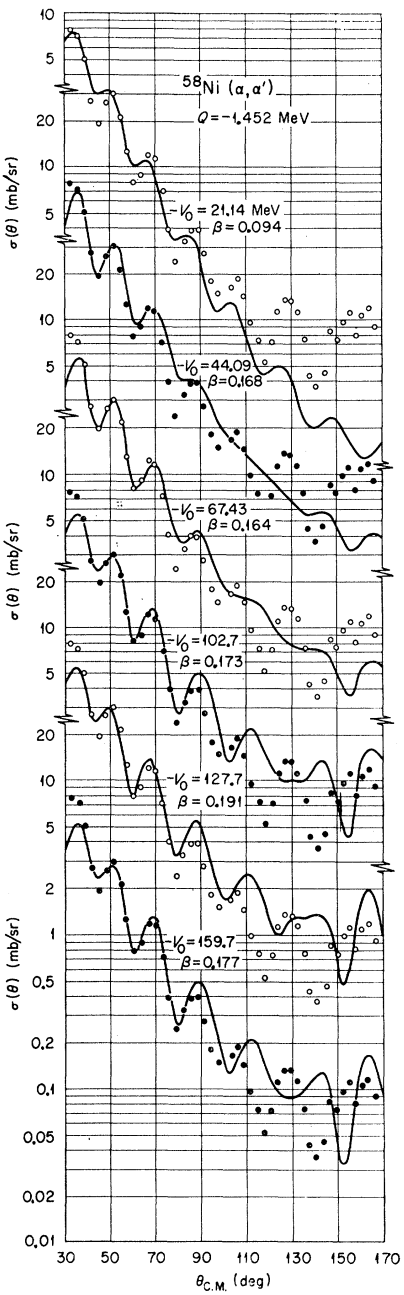

FIG. 8. Distorted-wave calculated angular distributions of inelastic scattering to first 2+ level in ^{58}Ni for six sets of parameters compared with the experimental data. The parameters are listed in Table VII. The values of the deformation parameters β were obtained by normalizing the calculated and experimental angular distributions at the maximum near 50 deg.

Calculated angular distributions for ^{58}Ni inelastic scattering to the first 2+ level at 1.452 MeV are compared with the experimental data in Fig. 8. Complex form factors were used and Coulomb excitation is included in the calculations. Values of the deformation parameter β are also shown. These values were obtained by normalizing the calculated angular distributions to the experimental data at the maxima near 50 deg.

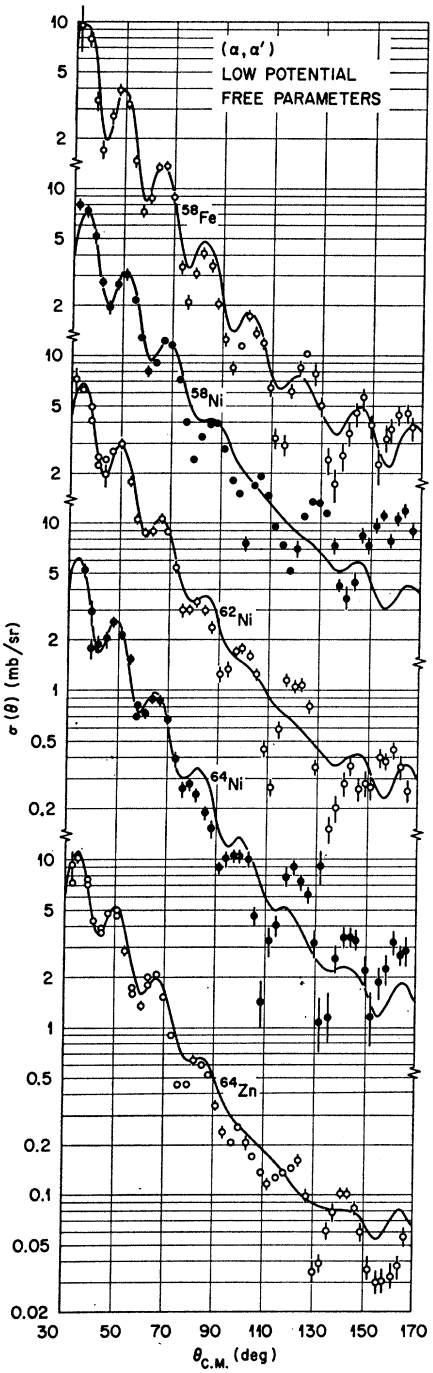

FIG. 9. Distorted-wave calculated angular distributions of inelastic scattering to first 2+ levels compared with experimental data. The parameters used are those obtained by the low-potential free-parameter searches which are listed in Table VI.

The calculated angular distributions shown in Fig. 8 reproduce the general features of the data at angles forward of ~100 deg. The phase agreement is good, and the falloff of the cross section with angle for the calculated curves is in good agreement with the data. Except for the $-V_0=21.14$ MeV potential the values of the deformation parameters β are equal to or lower than the value of 0.19 obtained from Coulomb-excitation data.[12] The values of β obtained for all except the $-V_0=21.14$ MeV potential in Fig. 8 agree reasonably well with the value of 0.18 obtained by Rost[8] for 43-MeV α inelastic scattering to the 2+ level in ^{58}Ni. It has been suggested[13] that βR_r is a more appropriate parameter with which to compare normalization constants from different theories. The values of βR_r are listed in Table IX.

TABLE IX. Values of βR_r for the various potentials from normalization of calculated and experimental angular distributions of first 2+ level in ^{58}Ni.

$-V_0$ (MeV)	βR_r
21.14	1.98
44.07	1.08
67.43	1.01
102.3	0.99
127.7	1.11
159.7	1.01
	0.92 (Coul exc)

This comparison of βR_r values suggests that the $-V_0=21.14$ MeV potential should be discarded although a minimum in χ^2 is obtained.

The principal difficulty with the distorted-wave angular distributions is that the agreement with the data ends at ~100 deg. The agreement between the calculated angular distributions and the data breaks down back of the angle where there is a change in slope of the envelope of the angular distributions. For the $-V_0=21.14$ MeV potential the phase agreement is good to ~140 deg but there is a large discrepancy in the magnitude of the cross sections, especially around 130 deg and larger angles. For the $-V_0=44.09$ MeV potential the distorted-wave calculation yields an angular distribution that is rather featureless for angles greater than 100 deg. For deeper real-well depths the featureless character at large angles is not observed but the phase agreement with the experimental data, that is obtained at forward angles, is not obtained at large angles.

The parameters obtained from the $C_1=$ const searches

[12] P. H. Stelson and Lee Grodzins, Nucl. Data, Sec. A 1, 21 (1965).

[13] J. S. Blair (private communication to E. Rost, cited in Ref. 8).

on ^{58}Ni were used in distorted-wave calculations of the inelastic scattering to the first 2+ level. These calculations yielded angular distributions that are out of phase with the experimental angular distributions at angles greater than ~80 deg. The over-all agreement thus obtained is not as good as that for the free-parameter searches (Fig. 8).

The optical-model parameters obtained from the low-potential and high-potential searches on the elastic data for the several targets (the parameters are listed

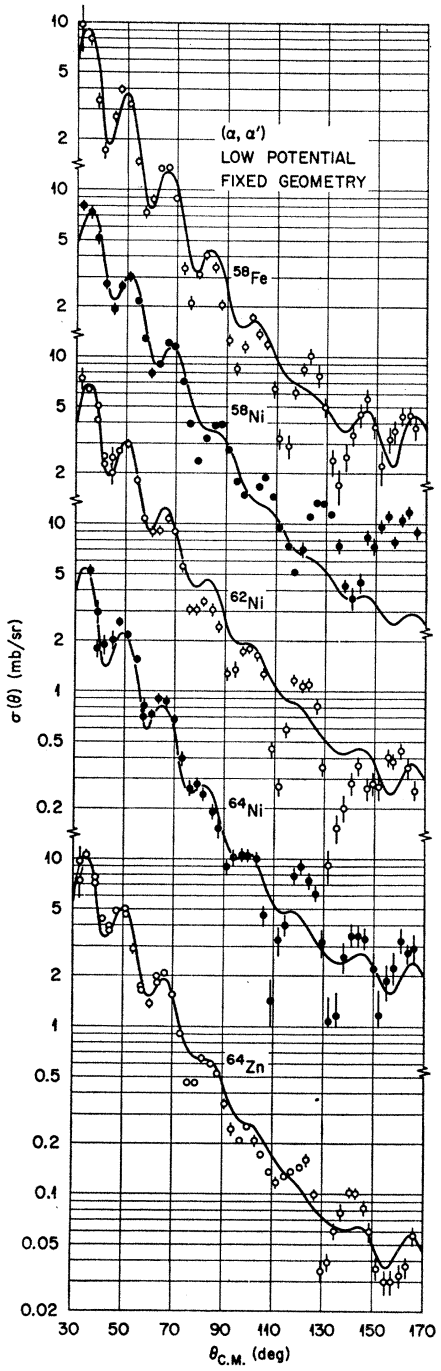

FIG. 10. Distorted-wave calculated angular distributions of inelastic scattering to first 2+ levels compared with experimental data. The parameters used are those obtained by the low-potential fixed-geometry searches which are listed in Table VI.

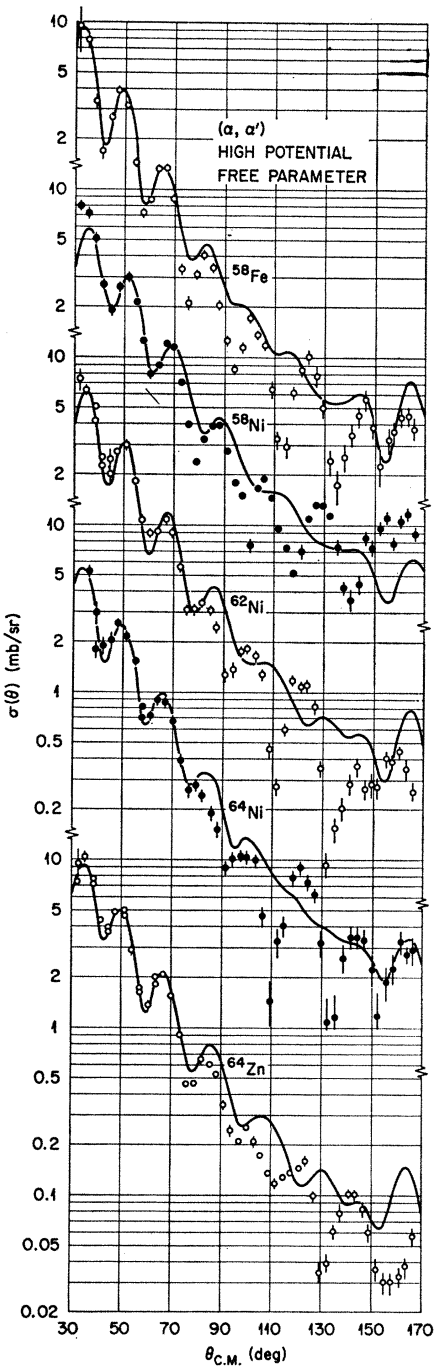

FIG. 11. Distorted-wave calculated angular distributions of inelastic scattering to first 2+ levels compared with experimental data. The parameters used are those obtained by the high-potential free-parameter searches which are listed in Table VI.

in Table VI) were used in distorted-wave calculations of the inelastic scattering first 2+ level angular distributions. As in the ^{58}Ni cases, complex form factors were used and Coulomb excitation was included. The calculated angular distributions are compared with the experimental data in Figs. 9–12. The values of the deformation parameter β, obtained from normalization of the calculated and experimental angular distributions at the maxima near 50 deg, are listed in Table VI. For comparison the values obtained from Coulomb-excitation data are also shown.

If we consider the low-potential free-parameters plot (Fig. 9) we observe that reasonable agreement is obtained for ^{58}Fe and almost as good agreement is obtained for ^{64}Ni. For the other targets the calculated angular distributions in Fig. 9 become featureless back of $\sim$100 deg. Following the ideas of Austern and Blair,[14] the behavior of these angular distributions can be crudely correlated with the reflection coefficients η_L for the elastic scattering. As seen in Fig, 13, the η_L curves for ^{58}Fe and ^{64}Ni have greater slopes in the region of η_L between 0.1 and 0.5 than for the remaining targets. Thus the transition amplitude is more sharply peaked in angular momentum space for these targets; this leads to a more diffractive structure in the angular distributions.

Examination of the phase shifts, e.g., for the low-potential free parameters and low-potential fixed geometry parameters for ^{58}Fe show negligible differences although the angular distributions obtained from distorted-wave calculations differ appreciably in the amplitude of the oscillations at large angles.

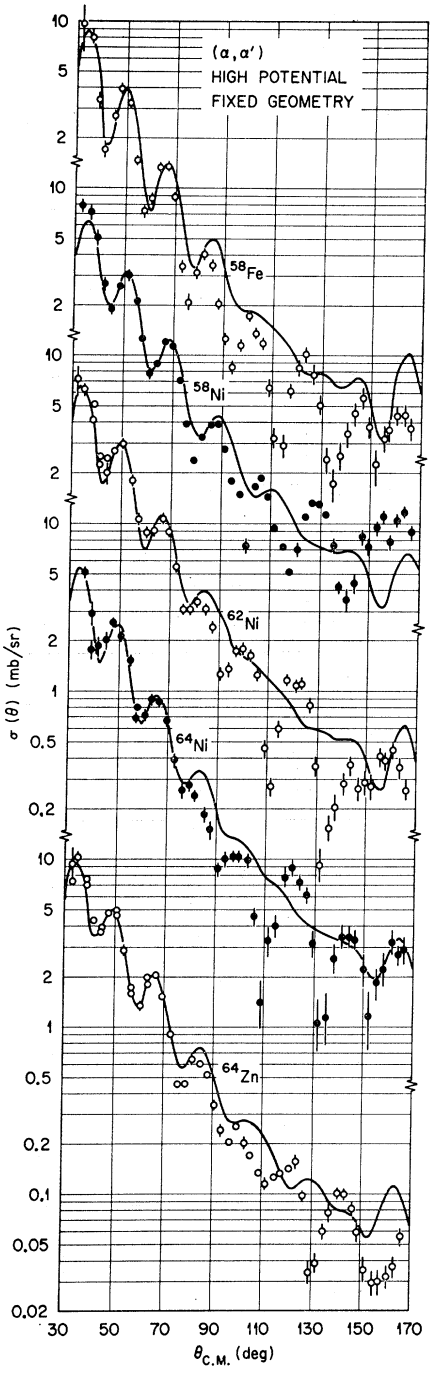

FIG. 12. Distorted-wave calculated angular distributions of inelastic scattering to first 2+ levels compared with experimental data. The parameters used are those obtained by the high-potential fixed-geometry searches which are listed in Table VI.

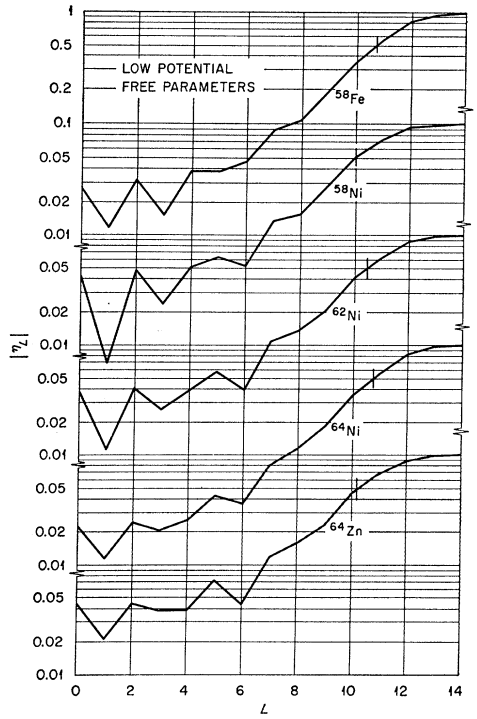

FIG. 13. η_L versus L for the low-potential free-parameter potentials

[14] N. Austern and J. S. Blair, Ann. Phys. (N. Y.) 33, 15 (1965).

COUPLED-CHANNEL CALCULATIONS

Coupled-channel calculations have been used[15] to fit data of elastic and inelastic scattering of α particles by Ni isotopes over the energy range of 25–100 MeV. While a through study was not attempted, we decided to explore coupled-channel calculations for the data reported here which is at a lower bombarding energy than that previously used for α scattering.

Coupled-channel calculations for ^{58}Ni were done with the families of optical parameters shown in Table VII. For these calculations the values of W_0, obtained from the optical-model search, were decreased by 30%. A value of 0.18 was used for the deformation parameter β. The computer time requirements did not permit parameter search for the coupled-channel calculation. Also in the interest of economy of computer time, Coulomb excitation was included for one case only.

An example of the coupled-channel calculations are compared with the experimental data in Fig. 14. The inelastic angular distributions predicted by several sets of optical-model parameters are compared with the experimental data in Fig. 15. For the $-V_0=44.09$ MeV case in Fig. 15 the angular distribution in which Coulomb excitation was included is also shown. It is apparent that Coulomb excitation makes an important contribution at forward angles to α inelastic scattering at 21-MeV bombarding energy.

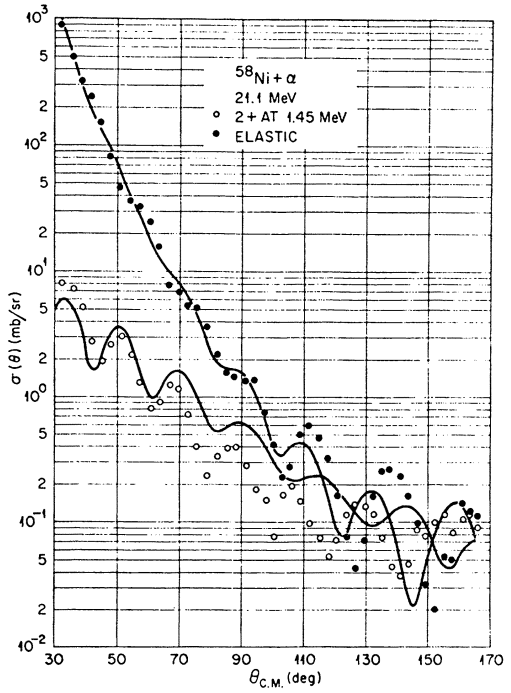

FIG. 14. Elastic and inelastic scattering angular distributions obtained from coupled-channel calculations compared with the experimental data. The parameters are those listed for the $-V_0=44.09$ MeV potential in Table VII with $-W_0$ decreased by 30%.

[15] T. Tamura, Nucl. Phys. 73, 81 (1965).

The elastic scattering predicted by the coupled-channel calculation is very similar to that of the optical-model calculation. A number of families of potentials give approximately equally good agreement with the data. The inelastic-scattering predictions of the coupled-channel calculation (Fig. 15) and the distorted-wave calculation (Fig. 8) are comparable at forward angles. They differ at large angles but neither agrees very well with the data at large angles. It is believed that suitable

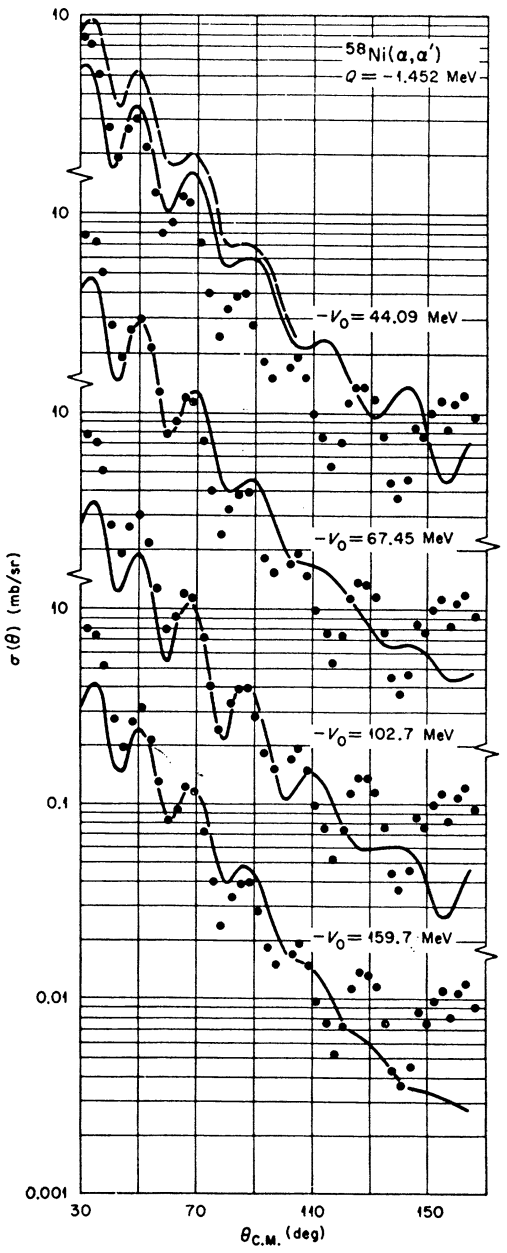

FIG. 15. Inelastic scattering angular distribution obtained by coupled-channel calculations compared with experimental data. The parameters are those listed for the respective real-well depth in Table VII with $-W_0$ decreased by 30%. Coulomb excitation was included in the calculation of the dashed curve only.

adjustments of parameters would improve the agreement at large angles.

DISCUSSION

The 21-MeV α-scattering data presented above have several features that are characteristic of surface reactions. One of the most prominent of these is that both the elastic and inelastic angular distributions exhibit well-defined oscillations throughout the range of the data. There are pronounced changes near 90° in the slope of the envelopes of the angular distributions, which according to Rost[8] are characteristic of surface reactions that are localized to a very few partial waves. The elastic and inelastic angular distributions are out of phase as predicted by the Blair phase rule,[7] which is based on the adiabatic approximation[16,17] for collective oscillations.

The analysis of the elastic scattering data indicate, however, that the scattering is also sensitive to the interior of the nuclear potential. Several sets of parameters (see Fig. 5 and Table VII) fits the ^{58}Ni data without a large range of χ^2. The quantities $C_1 = V_0 \exp(R_r/a_r)$ and $C_2 = M_0 \exp(R_w/a_w)$ are not constant, as would be expected if the elastic scattering were dependent only on the surface of the nucleus. Figure 7 demonstrates that only discrete values of real-well depth yield minima in χ^2.

Wilson and Sampson[3] analyzed 22-MeV α-scattering data from ^{56}Fe and three Zn isotopes with an optical model in which the radius and diffuseness parameters were of the same values for the real and imaginary wells. In that work, C_1 was required to have a constant value. For angles greater than 120° the agreement between optical-model predictions and the data was poor. In the optical-model analyses reported here, some variation in the real and imaginary geometrical parameters was permitted; in general, the agreement between optical-model predictions and the data is better at large angles than was reported in Ref. 3. The better agreement is principally in the phase of the oscillations. In Fig. 5 it is demonstrated that the restriction of $C_1 = \text{const}$ leads to poorer agreement between the optical-model predictions and the data.

The authors of Ref. 3 also imply that distorted-wave predictions of the inelastic scattering can be used to reduce the ambiguity of the optical-model potential that results from analysis of elastic-scattering data. They also favor the potentials that have real-well depths of ~20 MeV. In the work reported here the ambiguity in the real-well depth was not removed by calculations for the inelastic scattering. There appears to be very little evidence that a real-well depth of ~20 MeV is the one that best characterizes the optical-model potential for α particles.

The distorted-wave calculations of the inelastic scattering angular distributions, with Coulomb excitation included, yield good agreement with the data for angles forward of ~90°. The agreement both in phase of the oscillations and falloff of cross section with angle is as good as that previously obtained at higher bombarding energies, where extensive studies have been made.

The distorted-wave calculations reported here yield angular distributions that do not reproduce all of the features of the data at large angles. The falloff of cross section with angle agrees reasonably well with the data throughout the angular range. The regular oscillations that are observed throughout the angular range of the data are not reproduced by the distorted-wave calculations for large angles. This failure of the distorted-wave calculations to reproduce all of the features of the data occurs in angular regions where the elastic and inelastic cross sections are comparable in magnitude. One important assumption of the distorted-wave treatment is that elastic scattering is the dominant process and inelastic events can be treated as perturbations. This assumption is satisfied in the data reported here only for angles less than ~90°.

ACKNOWLEDGMENTS

We are indebted to R. H. Bassel for extensive discussions and suggestions during the analysis of the data. We are also grateful to R. M. Dirsko and G. R. Satchler for several discussions, and to T. Tamura for discussion and assistance in the coupled-channel calculations.

[16] D. M. Chase, Phys. Rev. **104**, 838 (1956).
[17] S. I. Drozdov, Zh. Eskperim. i Teor. Fiz. **28**, 734 (1955); **28**, 736 (1955) [English transls.: Soviet Phys.—JETP **1**, 591 (1955); **1**, 588 (1955)].